Article

Cell Reports

# RET Recognition of GDNF-GFRα1 Ligand by a Composite Binding Site Promotes Membrane-Proximal Self-Association

## Graphical Abstract

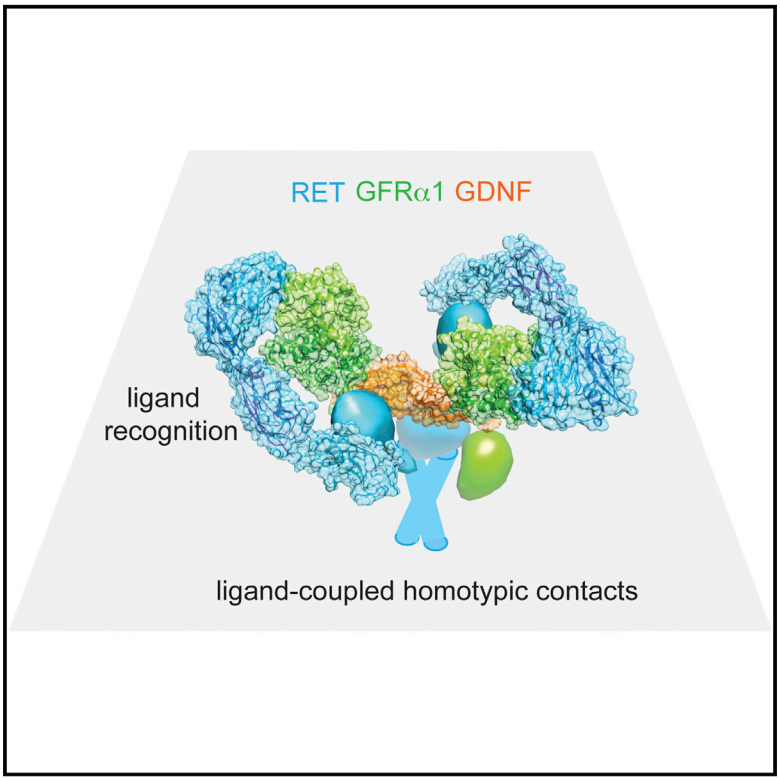


## Highlights

Extracellular architecture of $RET^{ECD}$ is revealed by SAXS

EM structure for a $RET^{ECD}$-GDNF-GFRα complex reveals a composite ligand-binding site

A GFRα1-binding hotspot contacts the invariant $RET^{CLD2-3}$ calcium sites

$RET^{CRD}$ couples ligand recognition and receptor homodimerization, exploited by MEN2A

## Authors

Kerry M. Goodman, Svend Kjær, ..., Edward P. Morris, Neil Q. McDonald

## Correspondence

neil.mcdonald@cancer.org.uk

## In Brief

RET is crucial for vertebrate development and causes three different human diseases. The basis for RET recognition of its bipartite GFL-GFRα ligands has been unclear. Goodman et al. describe a flower-shaped structure for a mammalian RET ectodomain-GDNF-GFRα1 complex. The structure reveals a composite binding site in RET that is driven by GFRα1 contacts and able to accommodate multiple GFL ligands. GFL-GFRα binding promotes a homotypic interaction between membrane-proximal regions of RET, a feature hijacked by oncogenic crosslinking mutations found in MEN2A patients.

## Accession Numbers

EMD-2712
EMD-2713
4ux8

Goodman et al., 2014, Cell Reports 8, 1894–1904
September 25, 2014 ©2014 The Authors
http://dx.doi.org/10.1016/j.celrep.2014.08.040

OPEN ACCESS
CellPress

Cell Reports
Article

# RET Recognition of GDNF-GFRα1 Ligand by a Composite Binding Site Promotes Membrane-Proximal Self-Association

Kerry M. Goodman,[1,6] Svend Kjær,[1,2,6] Fabienne Beuron,[3,6] Phillip P. Knowles,[1] Agata Nawrotek,[1] Emily M. Burns,[1] Andrew G. Purkiss,[1] Roger George,[2] Massimo Santoro,[4] Edward P. Morris,[3] and Neil Q. McDonald[1,5,*]
[1]Structural Biology Laboratory
[2]Protein Purification Facility
Cancer Research UK, London Research Institute, 44 Lincoln's Inn Fields, London WC2A 3LY, UK
[3]Division of Structural Biology, The Institute of Cancer Research, London SW7 3RP, UK
[4]Dipartimento di Biologia e Patologia Cellulare e Molecolare, Università di Napoli Federico II, via S. Pansini 5, 80131 Naples, Italy
[5]Institute of Structural and Molecular Biology, Department of Biological Sciences, Birkbeck College, Malet Street, London WC1E 7HX, UK
[6]Co-first author
*Correspondence: neil.mcdonald@cancer.org.uk
http://dx.doi.org/10.1016/j.celrep.2014.08.040


## SUMMARY

**The RET receptor tyrosine kinase is essential to vertebrate development and implicated in multiple human diseases. RET binds a cell surface bipartite ligand comprising a GDNF family ligand and a GFRα coreceptor, resulting in RET transmembrane signaling. We present a hybrid structural model, derived from electron microscopy (EM) and low-angle X-ray scattering (SAXS) data, of the RET extracellular domain ($RET^{ECD}$), GDNF, and GFRα1 ternary complex, defining the basis for ligand recognition. $RET^{ECD}$ envelopes the dimeric ligand complex through a composite binding site comprising four discrete contact sites. The GFRα1-mediated contacts are crucial, particularly close to the invariant RET calcium-binding site, whereas few direct contacts are made by GDNF, explaining how distinct ligand/coreceptor pairs are accommodated. The $RET^{ECD}$ cysteine-rich domain (CRD) contacts both ligand components and makes homotypic membrane-proximal interactions occluding three different antibody epitopes. Coupling of these CRD-mediated interactions suggests models for ligand-induced RET activation and ligand-independent oncogenic deregulation.**

## INTRODUCTION

RET is a single transmembrane-spanning receptor tyrosine kinase (RTK) that plays critical roles in the development of vertebrate central and peripheral (enteric) nervous systems, kidney and Peyer's patch organogenesis, and spermatogenesis (Ibáñez, 2013). RET is directly causal in several human diseases, including Hirschsprung's disease; congenital anomalies of the kidneys or lower urinary tract; and multiple cancers, including multiple endocrine neoplasia type 2A and 2B (MEN2A and MEN2B) syndromes (Amiel et al., 2008; Mulligan, 2014; Schedl, 2007). RET is the primary signaling receptor for glial-cell-line-derived neurotrophic factor (GDNF) family ligands (also known as GFLs), which are soluble covalent dimeric ligands and members of the cystine-knot superfamily (Airaksinen and Saarma, 2002). However, RET only recognizes GFLs bound to a member of the GDNF receptor alpha (GFRα) family of glycosylphosphatidylinositol (GPI)-linked coreceptors (Treanor et al., 1996; Trupp et al., 1996). There are four human GFLs: GDNF, artemin (ART), neurturin (NTN), and persephin, which combine with four human GFRα coreceptors to form cognate and noncognate pairs. Each pair is capable of binding and stimulating RET autophosphorylation at discrete tyrosine sites. This suggests a remarkable molecular plasticity within RET receptor to accommodate this diverse set of ligands. The RET-GFL-GFRα complex (the RET "ternary" complex) has a 2:2:2 stoichiometry and exhibits positive cooperativity (Schlee et al., 2006).

The ligand-binding RET ectodomain ($RET^{ECD}$) contains four consecutive cadherin-like domains (CLD1–CLD4) followed by a membrane-proximal cysteine-rich domain (CRD) (Figure 1A). RET CLD domains diverge significantly from classical cadherins (calcium-dependent adhesion) in sequence, structure, and arrangement (Anders et al., 2001; Brasch et al., 2012; Kjaer et al., 2010). $RET^{CLD1-2}$ forms a clamshell arrangement in marked contrast to the linear organization of tandem repeats of cadherin domains (Kjaer et al., 2010). Calcium ions are critical for RET folding consistent with the conservation of classical cadherin calcium-coordinating motifs between CLD2 and CLD3 (Anders et al., 2001; Kjaer and Ibáñez, 2003a; van Weering et al., 1998).

Efforts to map the bipartite GDNF-GFRα1-binding site within $RET^{ECD}$ have implicated almost the entire $RET^{ECD}$ region. Cross-linking studies suggested that the CRD domain makes direct contacts with both the GDNF ligand and GFRα1 molecule (Amoresano et al., 2005). A separate study identified several regions

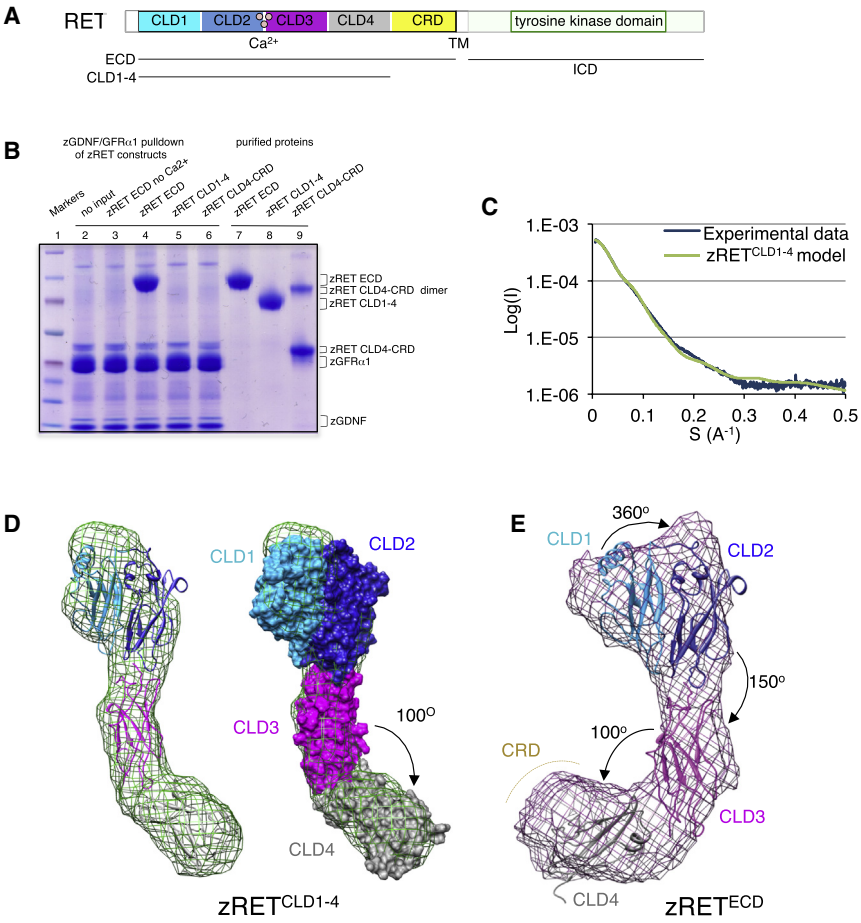


**Figure 1. Architecture and Ligand Binding Properties of zRET$^{CLD1-4}$ and zRET$^{ECD}$**

(A) RET domain organization, highlighting the extracellular domain (ECD) and domain color codes used throughout.

(B) Ligand binding properties of zRET$^{ECD}$, zRET$^{CLD1-4}$, and zRET$^{CLD4-CRD}$. Purified recombinant proteins were added to immobilized zGDNF-GFRα1 in the presence of calcium (except lane 3). Samples were visualized by Coomassie-stained SDS-PAGE.

(C) SAXS data for the zRET$^{CLD1-4}$. The solid line shows the scattering curve calculated from the RET$^{CLD1-4}$ model shown in (D), with a $\chi^2 = 3.1$.

(D) Ab initio SAXS reconstruction superimposed with a model for RET$^{CLD1-4}$ constructed as described in the text.

(E) Ab initio SAXS reconstruction for RET$^{ECD}$ compared with the model for RET$^{CLD1-4}$ produced in (D). A potential location for the CRD domain packing against CLD4 is indicated.

within RET$^{CLD1}$ that are important for ligand-coreceptor binding whereas characterization of human/*Xenopus* RET$^{ECD}$ receptor chimeras implicated human RET$^{CLD1-3}$ in restoration of binding to both mammalian GDNF-GFRα1 and NTN-GFRα2 complexes (Kjaer and Ibáñez, 2003b). Structure-function analyses on GFL-GFRα ligands have implicated residues within domains D2 and D3 of GFRα in binding RET (Parkash et al., 2008; Wang et al., 2006). These studies used structures of binary complexes of GFL-GFRα that lacked the related domain D1, thought to be dispensable for GDNF and RET binding (Scott and Ibanez, 2001).

Despite the importance of RET in vertebrate development and disease, the molecular basis for RET recognition of its bipartite GFL-GFRα ligands is not known. Here, structural models for reconstituted mammalian (mTC) and zebrafish (zTC) RET-GDNF-GFRα1 ternary complexes are presented and further validated by a Fab-complex reconstruction by zTC mutational assay and by probing monoclonal antibody epitopes in mTC. The flower-shaped structural model identifies how a composite binding site in RET involving multiple CLD domains and the CRD domain can accommodate multiple GFL ligands and drives a homotypic interaction between membrane-proximal regions of RET$^{CRD}$. Ligand engagement may organize CRD self-association triggering RET signaling, a property that is hijacked by crosslinking oncogenic mutations found in MEN2A patients.

## RESULTS

### Spatial Organization of the RET Extracellular Domain

Recombinant zebrafish RET extracellular domain (zRET$^{ECD}$) and cadherin-like domains 1–4 (zRET$^{CLD1-4}$) were prepared using baculovirus-mediated protein expression in insect cells. By size exclusion chromatography coupled multiangle light scattering (SEC-MALS), zRET$^{ECD}$ and zRET$^{CLD1-4}$ had apparent molecular weights of 83.7 and 67.5 kDa, respectively (Figures S1A and S1B). Partial deglycosylation of zRET$^{ECD}$ and zRET$^{CLD1-4}$ was achieved with endoglycosylase F1, resulting in monodisperse samples with reduced sugar content. To examine whether these proteins were functional in vitro, zRET$^{ECD}$, zRET$^{CLD1-4}$, and zRET$^{CLD4-CRD}$ proteins were tested for binding to zGDNF-zGFRα1a (referred to subsequently as zGFRα1) using a zTC reconstitution assay (Figure 1B). Only zRET$^{ECD}$ bound the ligand complex and only in the presence of calcium. Shorter constructs showed no detectable binding, indicating the entire RET$^{ECD}$ is required for ligand recognition similar to human RET$^{ECD}$ (Kjaer and Ibáñez, 2003b).

To obtain information on the molecular shape of both zRET$^{ECD}$ and zRET$^{CLD1-4}$ in solution, low-angle X-ray scattering (SAXS) data were collected (Figures 1C, S1C, and S1D). Pair distance distributions exhibited fine features consistent with a multidomain protein sample. Ab initio envelopes were generated for both zRET$^{ECD}$ and zRET$^{CLD1-4}$ using DAMAVER consistent with the pair distance distributions. Both showed an elongated shape and a similar radius of gyration. Zebrafish RET$^{ECD}$ data generated a twisted "horseshoe"-shaped object whereas the RET$^{CLD1-4}$ displays an "L"

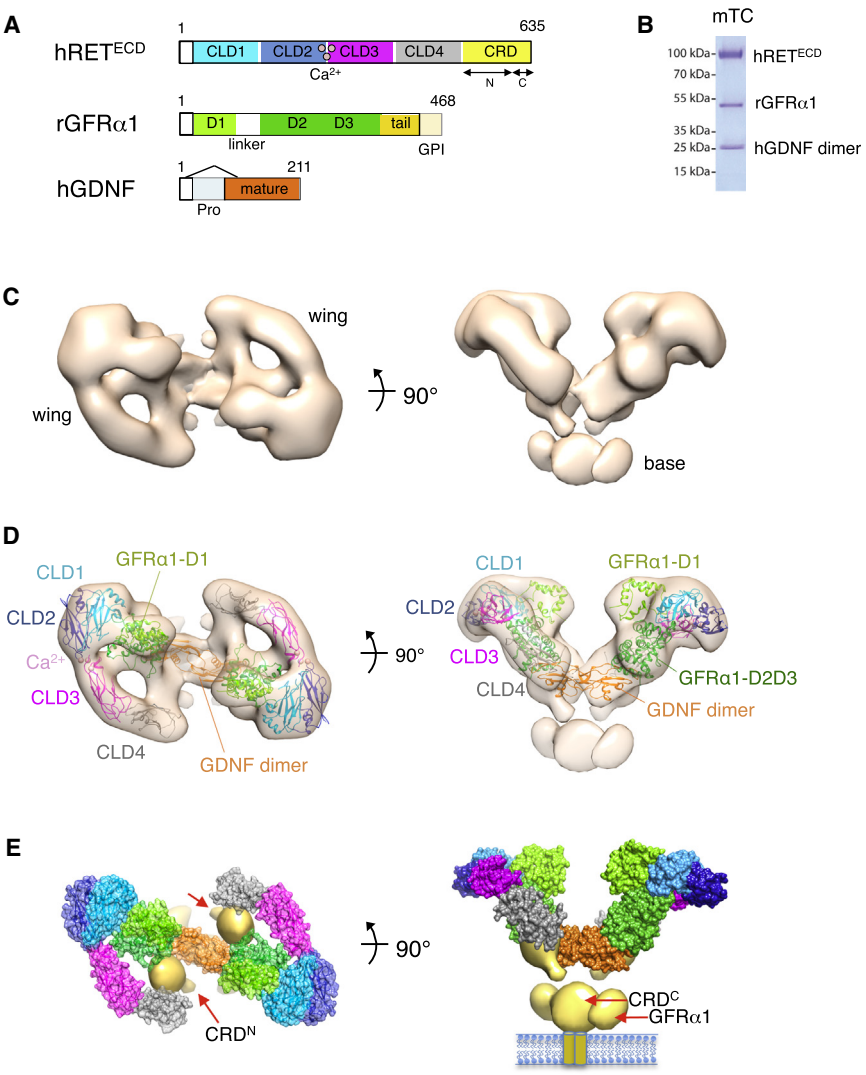


**Figure 2. Electron Microscopy Reconstruction of a Reconstituted Mammalian RET$^{ECD}$-GDNF-GFRα1 Ternary Complex**

(A) Domain schematic for RET$^{ECD}$, GDNF, and GFRα1 regions used to assemble mTC. The CRD region is further divided into an amino-terminal CRD$^{N}$ and carboxy-terminal CRD$^{C}$ portion (residues 591–627).

(B) SDS-PAGE of assembled recombinant mTC.

(C) Orthogonal views of the mTC 3D reconstruction at 24 Å resolution from negative-stain electron microscopy. The surface representation encloses a molecular weight of 264 kDa.

(D) Structural model for mTC generated by fitting various domains into the EM map as described in the text.

(E) Left: difference volume map (yellow) generated after fitting all mTC components (as in D, but represented as surface), showing the inferred location of the amino-terminal portion of the CRD domain (CRD$^{N}$). Right: the base density contains the GFRα1 carboxy-terminal tail and carboxyl-terminal residues from RET$^{CRD}$ prior to residue 635 (CRD$^{C}$), indicated by red arrows.

shape with a short and long arm with a wide "head" (Figures 1D and 1E). The addition of the CRD within RET$^{ECD}$ did not extend the maximum intramolecular vector length but generated a "bump" adjacent to RET$^{CLD4}$, which was tentatively attributed to part of the CRD.

The zRET$^{CLD1-4}$ structure was modeled using the human RET$^{CLD1-2}$ (hRET$^{CLD1-2}$) structure (Protein Data Bank [PDB] code 2X2U) and cadherin-based models for hRET$^{CLD3}$/hRET$^{CLD4}$. The hRET$^{CLD1-2}$ structure, with its distinctive clamshell shape, was recognizable at the wider end of the RET$^{CLD1-4}$ envelope (Figure 1D). A model for the RET$^{CLD3}$ domain was placed relative to RET$^{CLD2}$ by using a tandem classic cadherin domain template (PDB code: 1LW3) to preserve both the conserved calcium-coordinating ligand geometry (LDRE, DXD, and DEDD motifs; Figure S5C) and the presumed linear arrangement of RET$^{CLD2}$ and RET$^{CLD3}$. A RET$^{CLD4}$ domain model was added to RET$^{CLD1-3}$ with a bend angle of 100° consistent with the ab initio SAXS envelopes. The final residuals from fitting the theoretical curves derived from this RET$^{CLD1-4}$ model against the experimental curves gave a $\chi^2$ value of 3.1, indicating a reasonable agreement. The high-quality SAXS data were therefore sufficient to generate preliminary models for RET$^{ECD}$ and RET$^{CLD1-4}$, defining all pairwise CLD interdomain angles and a potential location for the CRD. The CLD2-CLD3 angle of 150° is within the range observed for tandem cadherin domains (130°–170°); however, given the lack of calcium ligands between CLD1-CLD2 and CLD3-CLD4, interdomain angles cannot be reliably predicted. The SAXS model indicates the CLD1-CLD2 clamshell resembles that of a calcium-free T-cadherin (Ciatto et al., 2010) whereas CLD3-CLD4 angle of 100° means CLD4 projects away from the CLD2-CLD3 principal axis.

## Reconstitution of mTC and zTC RET-GDNF-GFRα1 Ternary Complexes

Two recombinant RET ternary complexes were assembled for structural analysis. The mTC consisted of human RET$^{ECD}$ (residues 1–635), rat GFRα1 (residues 1–427, removing the GPI-attachment site), and mature human GDNF (residues 77–211; Figure 2A; Supplemental Information). Previous studies showed that hRET$^{ECD}$ produced in a glycosylation-deficient Chinese hamster ovary (CHO) Lec8 cell line binds to hGDNF-rat GFRα1 (rGFRα1) ligand with a $K_d$ of 15 nM (Kjaer et al., 2010). No interaction between RET$^{ECD}$ and hGDNF or rGFRα1 coreceptor individually was detectable (data not shown). The mTC was reconstituted in the presence of 1 mM calcium to give a pure and monodisperse sample with a molecular weight of 343 kDa by SEC-MALS (Figures 2B and S1E). The calculated molecular

weight of mTC, using a stoichiometry of two copies of $RET^{ECD}$: two copies of GFRα: one GDNF dimer, was 260 kDa, suggesting a substantial portion of the measured mass is contributed by glycosylation.

Separately, a zebrafish ternary complex ($zRET^{ECD}$-zGDNF-zGFRα1a) was also prepared consisting of $zRET^{ECD}$ (residues 1–626), zGFRα1a (residues 1–352), and zGDNF (residues 135–235; Figure S1F). These constructs were designed to truncate the carboxy-terminal 120-amino-acid tail of zGFRα1 (referred to as $GFR\alpha1^{delC}$) and the unstructured amino-terminal 46 amino acids of mature zGDNF (referred to as $zGDNF^{delN}$). The components formed a ternary complex (defined hereafter as $zTC^{min}$) that shows a size-exclusion profile similar to mTC (Figure S1F). However, by SEC-MALS, the $zTC^{min}$ appeared less homogeneous than mTC, with molecular weights ranging from 200 kDa to 420 kDa.

## 3D Reconstruction of a Mammalian RET-GDNF-GFRα1 Ternary Complex

The mTC complex was placed on electron microscopy (EM) grids, negatively stained, and analyzed by single-particle methods to obtain a 3D reconstruction. Molecular images of mTC revealed a range of different orientations of the complex and a good level of internal detail (Figure S2A). Reference-free classification gave a range of class averages from which two distinct views were extracted: (1) the "leg" view with two densities branching from a more diffuse base (Figure S2B) and (2) a "figure of eight" view (Figure S2B) with apparent 2-fold rotational symmetry. The multivariate statistical analysis performed on the complete non-rotationally aligned single particles data set shows eigen images with 2-fold symmetry (Figure S2C). A starting 3D model was built from two such classes assumed to correspond to almost orthogonal orientations of the particle on the grid. This initial model was further refined to produce the EM map shown in Figure 2C. The reliability of the map is attested by the good agreement between classes and reprojections (Figure S2D) and the even distribution of Euler angles (Figure S2E). The resulting map has a resolution of 24 Å as estimated by Fourier shell correlation (Figure S2F). The mTC complex measures 190 Å in its longer dimension and is made up of two elliptic domains ("wings") when viewed down the 2-fold rotational axis (Figure 2C, left), coalescing into a base domain (Figure 2C, right). When the density map is contoured at a threshold chosen to encompass a molecular weight of 264 kDa (calculated molecular weight of mTC), the map generally has good connections between adjoining domains but lacks a connection between the wings and the base. However, bridging density is visible when the threshold used encloses a volume equivalent to a molecular weight of 430 kDa and connects to the inner lobe of the base (Figure S3A).

## Generating an EM Structural Model for mTC

To construct an mTC structural model from the EM map, coordinates of the bipartite $GFR\alpha1^{D2\text{-}D3}$:GDNF dimeric ligand (PDB code: 3FUB) were placed into the 3D reconstruction by aligning the dyad symmetry axis of the GDNF-$GFR\alpha1^{D2\text{-}D3}$ crystal structure with the 2-fold symmetry axis of the EM map. Only one of the two possibilities gave a good fit with the EM map, namely GDNF closest to the base (as opposed to $GFR\alpha1^{D2\text{-}D3}$ toward the base; Figure 2D, right-hand view). This placed the bipartite ligand at the center of the mTC complex (Figure 2D). Next, $RET^{CLD1\text{-}4}$ could be readily identified on the outside (the wings) of the 3D reconstruction using the knowledge of the SAXS-derived model (Figure S3B). Fitting the $RET^{CLD1\text{-}4}$ SAXS-derived model into the EM 3D reconstruction closely preserved the interdomain CLD angles observed for $RET^{CLD1\text{-}4}$. The theoretical SAXS scattering curves derived from the EM model of $hRET^{CLD1\text{-}4}$ fit the observed SAXS curves better than the SAXS-derived $zRET^{CLD1\text{-}4}$ model (Figure S3C). This validated the SAXS model and confirmed the identity of this region of the EM 3D reconstruction. Finally, a homology model of the $GFR\alpha1^{D1}$ domain (derived from $GFR\alpha3^{D3}$) was placed into a prominent density adjacent to $RET^{CLD1\text{-}2}$ and next to $GFR\alpha1^{D2\text{-}D3}$ (Figure 2D). This gave a good fit and match to the estimated volume calculated from the D1 domain sequence. The L-shaped $GFR\alpha1^{D1}$ domain was oriented to place a conserved N-linked glycosylation site into solvent rather than in an opposite arrangement that would place the glycosylation site in an interface with $GFR\alpha1^{D3}$. The D1 domain placement is made with lower confidence than the rest of the mTC structural model due to this independent fit and orientation into the EM map (see Supplemental Information for a description). It gives a GFRα1 domain organization with $GFR\alpha1^{D3}$ flanked by both $GFR\alpha1^{D1}$ and $GFR\alpha1^{D2}$. The long, highly conserved D1-D2 linker most likely wraps around one side of $GFR\alpha1^{D2D3}$. Overall, a correlation coefficient (CC) of 0.84 between the mTC structural model at 24 Å with the EM map was indicative of the good agreement between model and density ($RET^{CLD1\text{-}4}$: CC = 0.87, GDNF-$GFR\alpha1^{D2\text{-}D3}$: 0.79, and $GFR\alpha1^{D1}$: 0.79). The EM map was therefore sufficient to develop a structural model for the mammalian RET ternary complex containing either known or readily modeled mTC domain structures.

Regions in the mTC map density not included in the structural model are shown in a difference density map (yellow surface, Figure 2E; Table S1). This map was calculated by subtracting the density for the structural model low-pass filtered to a resolution of 25 Å from the mTC map density. Two regions are evident: a globular density sandwiched between CLD4 and $GFR\alpha1^{D2}$-GDNF ligand (seen in Figure 2E, left panel) and a detached "base" region (Figures 2C and 2E, right panel). The first region is bilobal, the larger lobe forms part of a "shared" $GFR\alpha1^{D2}$-GDNF RET interface as described later. The smaller lobe projects toward the central density of the base region containing the 2-fold axis (Figure 2E). This difference map volume was estimated to correspond to about 12 kDa, leading to the assignment of the $RET^{CRD}$ domain ($CRD^{N}$; residues 509–600; Table S1) to this density consistent with its location close to the $RET^{CLD4}$, as suggested by the SAXS envelope for $RET^{ECD}$ (Figure 1E). The base region from the EM map has an inner volume around the 2-fold axis flanked by symmetry-related external volumes. Either could potentially contain the N terminus of mature hGDNF (residues 1–39; known to be unstructured), the C-terminal tail of GFRα1 (residues 353–427), or the C-tail of $hRET^{CRD}$ ($CRD^{C}$; residues 601–635). The inner volume of the base region was tentatively assigned to the C-tail of $RET^{CRD}$ based on volume estimates (Table S1) and the weaker connecting density observed at lower thresholds (Figure S3A, right panel). This

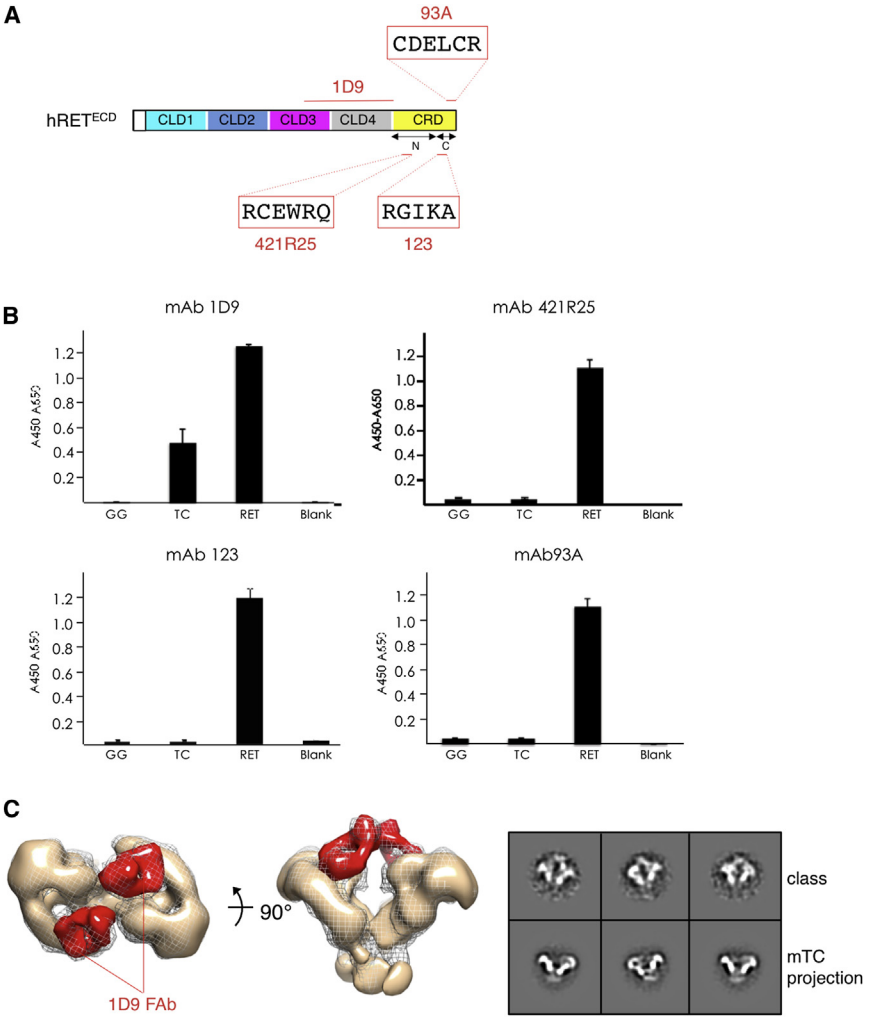


**Figure 3. mTC Structure Validation Using Antibody Epitope Mapping**

(A) Location of epitopes for four monoclonal antibodies mapped against $hRET^{ECD}$ (see Figure S4). The 1D9 monoclonal binds a conformational epitope within the CLD3-CLD4 linker and CLD4. Monoclonals mAb 421R25, mAb 93A, and mAb 123 recognize short linear epitopes within the $hRET^{CRD}$.

(B) ELISA assay to assess the accessibility of antibody epitopes in unliganded $RET^{ECD}$ and the mTC complex. Antibodies were added to wells coated with GDNF-GFRα1-Fc (GG), human RET ternary complex (TC), $RET^{ECD}$ alone (RET), and no protein control (blank). Error bars were calculated from the SE of the measurements. Three independent measurements were obtained per experiment.

(C) Left: orthogonal views of the 1D9 Fab-mTC EM reconstruction (mesh) showing fitting of the mTC EM reconstruction (beige surface) bound to two 1D9 Fabs (red surface). The Fab fragments were docked into the additional apical density at CLD3-CLD4, validating the mTC structure interpretation. Right: reference-free class averages of the mTC-1D9 Fab complex are shown (top row) with the matching forward projections of the mTC reconstruction (bottom row).

would indicate that the bottom of the base lies adjacent to the plasma membrane. The flanking outer base density (Figure 2E, right panel) was then assigned to the 120-residue C-tail of GFRα1. This interpretation is consistent with the $RET^{CRD}$ C-terminal residues being in close proximity, allowing the RET transmembrane helices (residues 636–660) to homodimerize as previously shown (Kjaer et al., 2006). Relaxing the C2 symmetry applied to mTC revealed some asymmetry in the base region but did not markedly change the main core of the mTC (Figure S3D).

In parallel to the mTC EM reconstruction, a data set was collected for the $zTC^{min}$ complex containing 7,510 particles using similar conditions to the mTC. The stability of the $zTC^{min}$ on EM grids was not as good as mTC, so the sample was cross-linked using glutaraldehyde to improve the sample homogeneity (Strauss and Wagenknecht, 2013). $zTC^{min}$-refined class averages and their corresponding reprojections closely resembled those obtained for mTC (Figure S3F). A 3D reconstruction for $zTC^{min}$ calculated using the mTC model as reference contained the same overall architecture for the ligand/coreceptor/$RET^{CLD1-4}$ with density for the D1 and CRD domains, but importantly, it lacked density for the base region (Figure S3G). This is consistent with the assignment of the C-terminal 120-residue tail of zGFRα1 within the base region, where it contributes to base stability.

## Validation of the mTC EM Structural Model

To further validate the mTC structural model, four anti-$RET^{ECD}$ monoclonal antibodies were characterized and their human $RET^{ECD}$ epitopes mapped by either immune blot or by immobilized peptide arrays (see Figure S4 for epitope mapping), summarized in Figure 3A. The monoclonal antibody (mAb) 1D9 antibody previously described (Salvatore et al., 2002) has a conformation-sensitive structural epitope between $RET^{CLD3}$ and $RET^{CLD4-CRD}$. An ELISA assay indicated that the epitope was accessible within both $hRET^{ECD}$ and the mTC complex (Figure 3B). In contrast, three other antibodies were found to have linear epitopes within the $hRET^{CRD}$, which could be recognized in a $RET^{ECD}$ context, but not within the mTC complex (discussed later). Therefore, Fab fragments derived from the mAb 1D9 were used to obtain an EM reconstruction of a Fab-labeled mTC complex. This complex was prepared and applied to EM grids in the same manner as the mTC alone. The Fab 1D9-labeled mTC sample gave rise to distinctive reference-free classes (Figure 3C, right panel), which were matched with references consisting of forward projections calculated from the mTC alone map. The resulting reconstruction showed good density consistent with two symmetrically bound 1D9 Fabs that mapped accurately to the density assigned to $RET^{CLD3}$ and $RET^{CLD4}$ on the exterior of the wings (Figure 3C). This demonstrated that the wing was

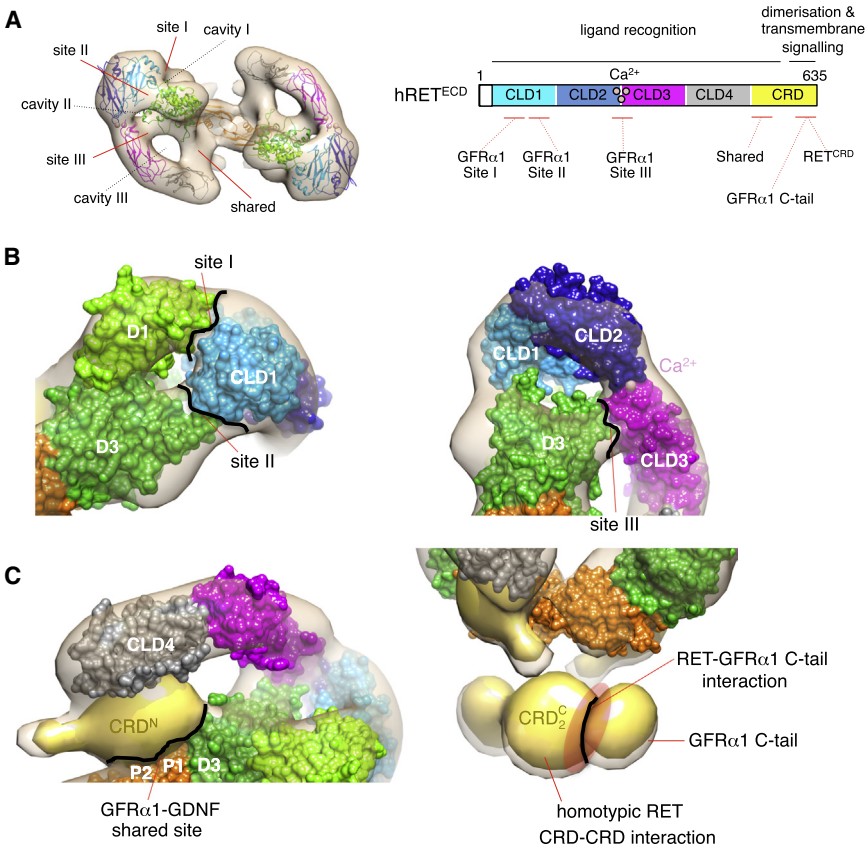


**Figure 4. Bipartite Ligand Recognition by hRET$^{ECD}$ Shows a Composite Binding Site**

(A) Contact surfaces within the EM structural model for mTC labeled with the EM map superposed (beige). Right panel: schematic of the contact sites within RET.

(B) Left panel: close up of site I and site II. Bold black line roughly delineates the contact surface. Right panel: close up of site III.

(C) Left panel: close up of the shared GDNF-GFRα1 contact surface highlighting the difference volume assigned to the CRD domain (yellow). Right panel: close up of the base region difference volume (yellow) assigned to CRD and GFRα1 C-tail.

correctly assigned to RET$^{ECD}$ and was correctly oriented. Validation of the mTC model allows a proper description of the arrangement of its component parts and confirms the placement of the plasma membrane at the bottom of the view of mTC in Figure 2E (right-hand panel).

## A Composite Binding Site for Bipartite Ligand within the mTC Structure

The mTC structural model reveals how GDNF-GFRα1 ligand is captured by RET$^{ECD}$ and drawn into close proximity to the membrane (Figure 4A). It also shows that the major RET$^{ECD}$ contacts are with the GFRα1 subunit and RET$^{ECD}$ makes very limited interactions with GDNF ligand. There are four major heterotypic contact sites (i.e., between bipartite ligand and RET$^{ECD}$) within the mTC structure, defined hereafter as sites I, II, III, and the fourth as a shared ligand/coreceptor site. The sites are designated from the RET$^{ECD}$ amino terminus to carboxy-terminal residue R635 and are discussed in more detail below. It is notable that sites I, II, and III contact RET$^{CLD1-3}$, consistent with the extended ligand-binding surface proposed from human/*Xenopus* chimeric RET experiments (Kjaer and Ibáñez, 2003b). A fifth heterotypic site is inferred between GFRα1 C-tail and RET$^{CRD}$ within the mTC base region, together with a homotypic RET$^{CRD}$ interaction that is discussed later. The contact surfaces are separated by substantial cavities within the mTC, and some regions, such as RET$^{CLD4}$, appear to make no direct contacts to ligand-coreceptor at all.

Both sites I and II involve RET$^{CLD1}$, the most divergent RET CLD, which contains residues and secondary structural elements previously identified as being unique to higher vertebrates (Kjaer et al., 2010). RET$^{CLD1}$ is pincered by independent contacts from loop1 of GFRα1$^{D1}$ (site 1—lower confidence, as discussed earlier) and loop1 from GFRα1$^{D3}$ (site II—high confidence; Figures 4B and S5A). Neither of these loops contains invariant GFRα residues, and the GFRα4 family member lacks a domain D1 altogether. The GFRα1$^{D1}$ contact centers on residues separating the CLD1 ßF strand and the *cis*-Pro disulfide-constrained loop. This sequence was disordered within the isolated CLD1-CLD2 structure. GFRα1$^{D3}$ engages both a loop that follows RET$^{CLD1}$ helix α1 and β strands ßC'/ßC'' (Figure 3B). In site II, GFRα1$^{D3}$ loop 1 is known to be flexible, as it adopts different conformations in two GDNF-GFRα1 structures (PDB codes: 2V5E and 3FUB). Site III is a high-confidence site from the mTC structural model. It contains conserved residues N-X-X-E/D-E/D motif between loop 3 and α10 helix of GFRα1$^{D3}$ and several regions proximal to the calcium-binding site between RET$^{CLD2}$ and RET$^{CLD3}$ (Figures 4B and S5C). GFRα1$^{D3}$ loop 3 is flanked by two disulfide-linked cysteines and is significantly longer than equivalents in domains D1 and D2. Similarly, contacts within RET$^{ECD}$ lie spatially close to the calcium-binding motifs D-E-D-D and E-N (Figure S5C). A second loop in RET$^{CLD3}$ adjacent to the D-X-D motif also faces toward the GFRα1$^{D3}$ surface. Contacts close to these calcium ligands are even more intriguing because calcium is essential for mTC assembly, an observation previously interpreted to reflect calcium's structural role in RET$^{ECD}$ stability. The shared site (high confidence) consists of surfaces from both protomers of the GDNF dimer as well as loop1 from GFRα1$^{D2}$ (Figure 4C). These regions face toward the larger difference density lobe interpreted as containing part of RET$^{CRD}$. The GDNF site involves residues G54–E58 (GLGYE) from α1 helix of one protomer and the edge of the GDNF "fingers" from the second protomer (Figure S5B). Loop1 from GFRα1$^{D2}$ spans residues C178–C189 between helices α2 and α3 and are generally poorly conserved among GFRαs.

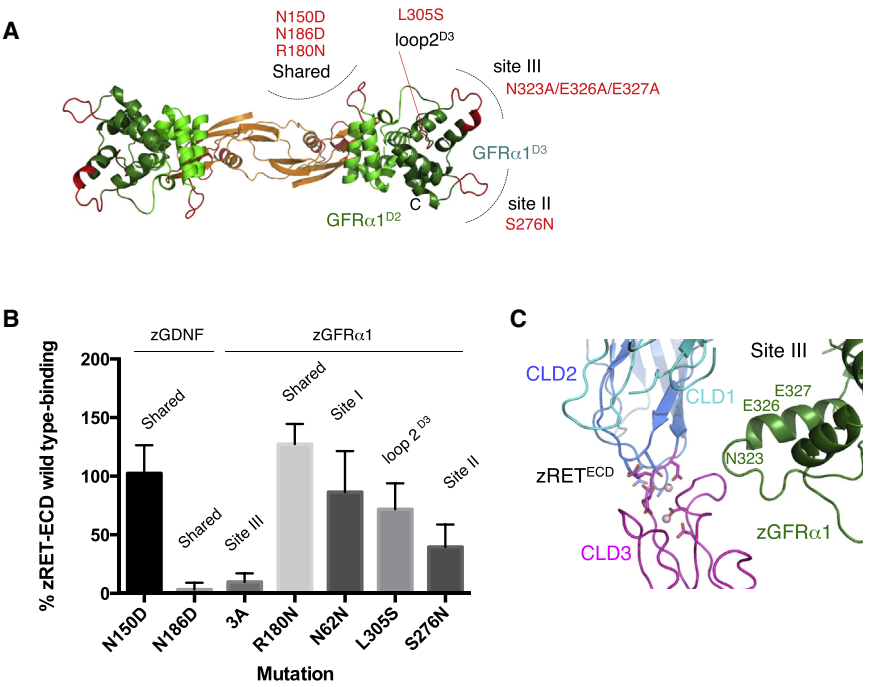


**Figure 5. Mutational Analysis Identifies a Crucial RET-Binding Hotspot within GFRα1 Adjacent to the RET$^{CLD2\text{-}CLD3}$ Calcium-Binding Region**

(A) Location of residues chosen for mutation within the zGDNF-zGFRα1 complex. N-linked glycosylation sites were added or deleted within each contact site to perturb binding, except for site III, which was tested by a triple-point mutation. Mutants were assessed for their ability to reconstitute a functional zTC in the presence of calcium.

(B) Quantification of zRET$^{ECD}$ binding to immobilized zGFRα1-zGDNF or mutant complexes. Three to four independent experiments were performed for each mutant, using three to four separate protein preparations. Nonspecific RET$^{ECD}$ binding was assessed in the absence of calcium and was <5% of total binding. The N186D zGDNF mutant was misfolded but is included to show no detectable binding to zRET$^{ECD}$ occurs in the absence of zGDNF. Error bars were calculated using the SEM from three to four independent experiments.

(C) Close up of the site III contact, highlighting the three residues mutated that are crucial for mTC assembly.

To probe the contribution of the mTC contact regions on RET ternary complex assembly, N-linked glycosylation sites (N-X-S/T) or point mutations were introduced or deleted within zGDNF ligand or zGFRα1 and assessed in a zTC$^{min}$ reconstitution assay (Table S2). The zTC$^{min}$ context was more amenable to a structure-function mutation analysis than mTC, given the complexity of producing mTC components in stable CHO cell lines. Mutations in zGDNF ligand or zGFRα1 coreceptor were designed to sample each of the four contact surfaces through surface loops or structural elements (Figure 5A). They were tested for their ability to bind equivalent levels of zRET$^{ECD}$ and reconstitute a zTC$^{min}$ complex. Residues tested were mostly conserved between zGFRα1-zGDNF and hGFRα1-hGDNF (Figure S5). The mutant zGFRα1-zGDNF proteins exhibited very different effects on zTC$^{min}$ complex formation (Figure 5B). A triple-alanine mutation in site III of zGFRα1 (N323A/E326A/E327A) adjacent to the CLD2-CLD3 calcium-binding site essentially abolished interaction with zRET$^{ECD}$ (Figures 5B and S6). A site II mutation (S276N) introducing a glycosylation site also significantly reduced binding by 60%. A loop2$^{D3}$ mutant (L305S) also had a markedly lowered affinity for zRET$^{ECD}$. Addition of a glycosylation site in loop1$^{D2}$ of zGFRα1 (R180N), located within the shared ligand/coreceptor site, actually increased affinity to 130%. Mutations that removed existing N-linked glycosylation sites from either zGDNF (N150D) at the shared site or at the site I interface with GFRα1 (N62D) had essentially wild-type binding consistent with previous studies, indicating sugar is not essential for complex assembly (Kjaer and Ibáñez, 2003b). Loss of these N-linked sites could be observed by SDS-PAGE (Figure S6). Overall, these data indicate that site II and site III mutations impact significantly on zRET$^{ECD}$ binding affinity.

## CRD Is Buried within mTC and Couples Ligand Recognition with Receptor Self-Association

In the mTC structural model, the CRD domain participates in both a shared ligand/coreceptor contact surface and a homotypic interaction with a second CRD domain apparently stabilized by a flanking C-tail from the GFRα component. To investigate the RET$^{CRD}$ further, three anti-hRET$^{ECD}$ antibodies whose linear epitopes were mapped to the CRD were used to probe epitope accessibility within mTC (Figure 3A). Antibody mAb 421R25 was found to recognize a linear epitope within hRET$^{ECD}$ that mapped to residues 540–545 (RCEWRQ) in the amino-terminal part of RET$^{CRD}$ (Figure S4). This epitope mapped to part of the hRET$^{CRD}$ packed against CLD4 and the shared site contacting GDNF-GFRα1 (Figure 2E). Using an ELISA-based assay, the mAb 421R25 epitope was found to be inaccessible within the mTC but exposed in hRET$^{ECD}$, indicating that this part of the CRD is buried upon ligand engagement (Figure 3B). A second antibody mAb m123 produced in house recognized a linear epitope containing residues 600–604 (RGIKA) from hRET$^{CRD}$ (Figure S4). This portion of hRET$^{CRD}$ is in the C-terminal tail of CRD (residues 600–635) buried within the homotypic hRET$^{CRD}$ interface of the base region (Figure 4C). This CRD epitope was found to be exposed to mAb m123 within hRET$^{ECD}$ but is blocked within mTC (Figure 3B), consistent with the CRD C-tail being buried within the mTC complex. A third antibody, mAb 93A (also produced in house), recognized a linear hRET$^{CRD}$ epitope containing residues 630–634 (CDELCR) at its most membrane-proximal extremity (Figure S4). This epitope is also masked within the mTC (Figure 3B). Intriguingly, this antibody does not bind the epitope in the presence of reducing agents, indicating that it selectively recognizes a C630-C634 disulfide epitope (Figure 6A). Therefore, evidence from three different

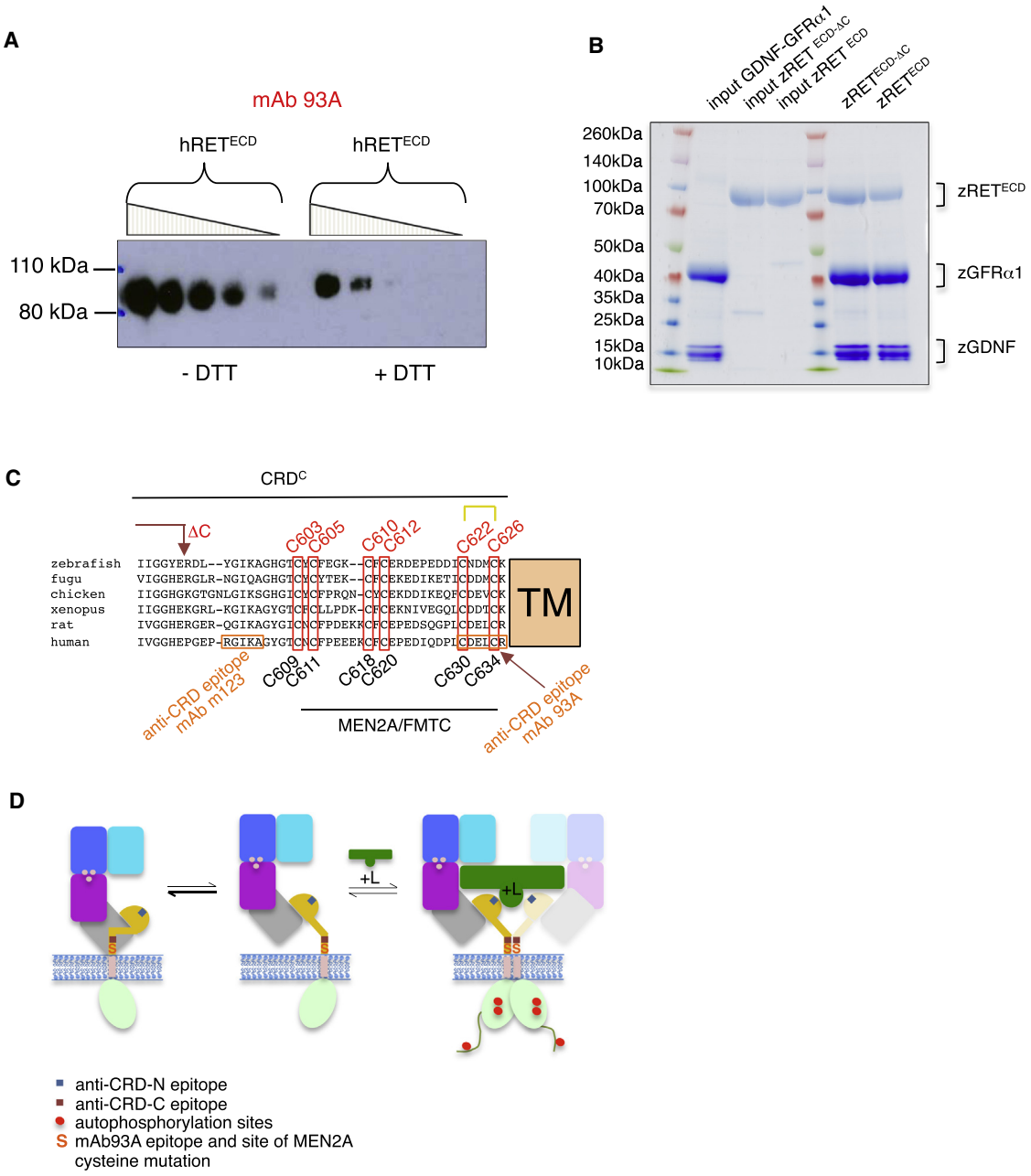


**Figure 6. A Membrane-Proximal CRD Region Mediates Homotypic Interactions Driven by RET Ligand Engagement**

(A) Western blot analysis of mAb 93A binding to a hRET$^{ECD}$ disulfide epitope (residues 630–635) in the presence or absence of reducing agents. Load from left to right was 0.5 μg, 0.25 μg, 0.125 μg, 0.0625 μg, and 0.031 μg hRET$^{ECD}$. DTT, dithiothreitol.

(B) SDS-PAGE gel of a pull-down of zRET$^{ECD}$ or zRET$^{ECD-\Delta C}$ using immobilized zGDNF-GFRα1, showing enhanced binding in the absence of residues 591–627. Gel quantification indicates 135% ± 10% relative to normalized binding by zRET$^{ECD}$. Three independent experiments were performed.

(C) Selected RET$^{CRD}$ sequences close to the transmembrane region, highlighting the cysteine residues targeted for oncogenic mutation in MEN2A/FMTC and the location of antibody epitopes for mAb 93A and m123.

(D) A schematic model for bipartite ligand (green, labeled L) interaction with RET, promoting homotypic dimerization of the RET CRD domain and activation. The GFRα1 tail contacts with CRD are omitted for clarity.

antibody epitope probes consistently indicates that the CRD is fully accessible within hRET$^{ECD}$ but is entirely buried within the mTC, up to and including its C-terminal residues prior to the transmembrane region.

To examine the ability of CRD to promote homotypic RET self-association independent of ligand, both hRET$^{ECD}$ and hRET$^{ECD}$ MEN2A (C634R), the most common RET mutation found in MEN2A patients (thought to generate crosslinked

disulfide-linked dimers), were examined for evidence of dimerization in solution. However, neither hRET$^{ECD}$ nor hRET$^{ECD}$ MEN2A (C634R) spontaneously formed dimers, even at high concentrations (Figure S1B; data not shown). To test whether the RET$^{CRD}$ C-terminal region influenced ligand interaction, residues 591–627 were deleted from zRET$^{ECD}$ (zRET$^{ECD-\Delta C}$), and this construct was tested in the in vitro pull-down assay (Figure 6B). Elimination of residues 591–627 significantly enhanced binding to zGDNF-GFRα1 (135% relative to normalized binding to wild-type zRET$^{ECD}$), indicating CRD homotypic interactions reduced the overall binding affinity for zGDNF-GFRα1 complex. This suggests that bipartite ligand binding must overcome resistance to self-associate mediated by the RET$^{CRD}$ C-terminal region (CRD$^{C}$). Overall, these data provide evidence that ligand recognition serves to crosslink two RET$^{ECD}$ molecules driving receptor self-association between CRD domains and most likely the transmembrane helix.

## DISCUSSION

The RET$^{ECD}$ organization described here indicates a substantial interdomain interface not only between domains CLD1 and CLD2 but between CLD4 and CRD. Both interfaces are consistent with observed mutual folding dependencies for each domain pair (i.e., they only fold correctly when expressed together; Kjaer and Ibáñez, 2003a). Interdomain angles for RET deviated significantly from those previously predicted (Anders et al., 2001), except for the CLD2-CLD3 angle, which resembles a classical calcium-binding cadherin arrangement. The SAXS-derived model for RET$^{ECD}$ aided an EM-derived structural model of a reconstituted mammalian RET-GFRα1-GDNF complex (“RET ternary complex,” abbreviated mTC), revealing the basis for bipartite ligand recognition. The mTC structural model was validated in several ways. These include EM single-particle reconstructions of a Fab-labeled ternary complex and a RET ternary complex from *Danio rerio* (zTC), together with site-specific mutational analysis and an ELISA probing anti-RET antibody epitope accessibility.

The mTC structural model reveals that the GFL ligand is captured beneath the GFRα coreceptor, close to the membrane. RET$^{ECD}$ wraps around and shields both the GFL ligand and coreceptor rather than projecting away from the plasma membrane. Limited contacts observed between RET and GFL ligand could accommodate any of the four GFLs when combined with a GFL-dimerized GFRα component. The mTC structural model rationalizes several previous studies indicating all RET$^{ECD}$ domains are required for a functional GDNF-GFRα1-binding site. The explanation is a synergy of distributed binding hotspots with mutual domain-folding dependencies. A binding hotspot between CLD2 and CLD3 is necessary (but not sufficient) to engage bipartite ligand, whereas the CRD is also required but is not sufficient for mTC assembly. CLD1 is essential for CLD2 folding, and CLD4 is required for CRD folding. Combining both RET$^{ECD}$ domain-folding dependencies with the location of ligand-binding hotspots prevents any single domain being dispensable for ligand interaction. The observed composite ligand-binding site contrasts sharply with other RTK-ligand structures that show a much more continuous, often domain-confined, surface to engage ligands (Lemmon and Schlessinger, 2010). It is more analogous to cytokine-receptor systems where individual cytokines have specialized receptors, a shared/common signaling receptor component, and composite binding sites (Stauber et al., 2006; Wang et al., 2005). Furthermore, these systems also offer precedents for the recognition of divergent ligands, such as the degenerate gp130 receptor that recognizes ciliary neurotrophic factor, leukemia inhibitory factor, and interleukin-6 cytokine ligands (Boulanger et al., 2003). The mTC structure suggests an unusual RTK recruitment mechanism more akin to cytokine-receptors complexes but driven by coreceptor GFRα1 engagement.

The mTC structural model also explains how hRET$^{CLD1-3}$ confers hGDNF-hGFRα1 binding specificity onto a human/*Xenopus* RET$^{ECD}$ chimera by preserving determinants for sites I, II, and III whereas permitting the self-associating CRD to come from a *Xenopus* RET origin (Kjaer and Ibáñez, 2003b). Binding determinants for hGDNF-hGFRα1 binding within CLD1 are particularly important (Kjaer and Ibáñez, 2003b). Satisfyingly, all but one of these CLD1 determinants appears to contribute directly to ligand-binding sites I/II/III in the mTC structural model (Figure 3). The exception is the amino-terminal β strand (residues 32–37) that is buried within the CLD1-CLD2 interface (Kjaer et al., 2010). Despite the composite nature of the interaction, a critical and conserved GFRα-binding energy “hotspot” is identified at site III, involving the motif N-X-X-E/D-E/D from domain D3. The GFRα contacts lie adjacent to the hRET$^{ECD}$ calcium-binding site between CLD2 and CLD3. This suggests the calcium dependence is not only crucial for RET folding but is also critical for ligand recognition, a feature that has been previously overlooked. Evolutionary pressure to preserve calcium ligands in RET only between CLD2 and CLD3 may reflect a need to retain a functional ligand-binding site. Previous studies predicted a RET-binding site based on an ART-GFRα3 structure but lacked supporting experimental evidence (Wang et al., 2006) or identified many potential RET-binding residues from different regions of the GFRα1 coreceptor (Parkash et al., 2008). These data need revisiting in view of the EM structural model described here. For example, GFRα1 D3 residues R190/R197, R257/R259, and K194/Q198/K202 (human GFRα1 numbering) were all implicated in RET binding but map to an interface with the GFRα1 D1 domain in the EM structural model. These residues constituted a putative heparin-binding site, leading the authors to suggest that heparin could inhibit RET signaling by binding to this surface. Alternatively, perturbing the D1 interface could affect RET engagement. Other residues such as E323/D324 (equivalent to zRET E326/E327, the site III hotspot) were correctly proposed but only now have a proper understanding as to how they contact RET (Parkash et al., 2008; Wang et al., 2006).

Probing three separate RET$^{CRD}$ epitopes with different monoclonal antibodies indicates they are buried within the mTC complex. The different locations of these RET$^{CRD}$ epitopes, two within CRD$^{C}$ (CDELCR and RGIKA), suggested that joint recognition of coreceptor and ligand promotes RET$^{CRD}$ C-tail self-association, assisted in part by the C-tail of GFRα1. The RET$^{CRD}$ C-tail homotypic interaction is the only source of direct dimerization contacts visible between RET dimers in the mTC. Deleting the CRD$^{C}$ increases ligand interaction, suggesting the

membrane-proximal region of RET may negatively influence ternary complex formation. It could act as a failsafe to block inappropriate ligand-independent receptor activation, similar to findings reported for the VEGFR2 receptor tyrosine kinase (Brozzo et al., 2012). EM class averages suggest the $RET^{CRD}$ is a relatively flexible region that is discernably separated from the core of the mTC complex. Previous data showed a strong self-association of the hRET transmembrane region (Kjaer et al., 2006), placing a tight constraint that the last CRD domain residue, R635, that precedes the transmembrane region must be in close proximity to a second RET receptor in the ternary complex. The absence of a base region in $zTC^{min}$ containing a GFRα1 C-tail truncation mutant uncovers a detectable but noncritical role for the GFRα1 C-tail in zTC assembly, warranting further characterization.

Ligand-driven self-association of $RET^{CRD}$ within mTC may account for the observed positive cooperativity (>80-fold) for recruiting a second RET molecule into the ternary complex after ligand engagement (Schlee et al., 2006). This is consistent with a stepwise assembly of mTC. $RET^{CRD}$ C-tail self-association is also fatally exploited in oncogenic forms of RET in MEN2A patients. Many RET mutations found in MEN2A patients lie in the C-terminal region prior to the membrane (C609Y/W, C611S/W, C618S/R/G/F/Y, C620R/W/F/S/Y, C630F, and C634R/W/F/S/Y/G; see Figure 6B), the most common being C634R at the end of $hRET^{CRD}$ (Waguespack et al., 2011). This mutant readily forms disulfide adducts in cells, leading to constitutive RET activation (Santoro et al., 1995). Covalent crosslinking of $CRD^{C}$ would potentially bypass a ligand requirement for self-association. However, neither $hRET^{ECD}$ nor its MEN2A equivalents form covalent or noncovalent dimers in solution. This can be rationalized by the lack of a cell membrane environment (3D versus a 2D diffusion), as the RET transmembrane region in known to promote self-association (Kjaer and Ibáñez, 2003a; Kjaer et al., 2006). Alternatively, it could also be explained by a ligand-dependent conformational change within $RET^{CRD}$ (Figure 6C). Such an allosteric model would require engagement of all four RET contact sites by ligand and coreceptor in order to reorient CRD correctly to promote self-association and activation. Whether such ligand-driven changes can alter the arrangement of RET transmembrane dimers requires investigation but is plausible. Although $RET^{CLD1-4}$ does not appear to grossly alter its conformation on ternary complex formation (comparing the SAXS-derived and EM-derived $RET^{ECD}$ model; Figure S3C), the CRD domain conformation appears more labile and could be susceptible to conformational changes. The mTC structural model and knowledge of antibody epitopes buried within the mTC suggests that specific reagents targeting the $RET^{CRD}$ may have therapeutic application in a subset of RET-driven cancers.

## EXPERIMENTAL PROCEDURES

### Protein Production and TC Assembly

Human $RET^{ECD}$ (residues 1–635; $hRET^{ECD}$) was expressed in stably transfected CHO Lec8 cells as a cleavable protein A fusion protein as described in Kjaer et al. (2010). Rat GFRα1 (residues 19–427, following signal sequence cleavage; rGFRα1) was also expressed in CHO cells. Mature human GDNF (residues 77–211; hGDNF) was from Amgen. For mTC assembly, excess hGDNF was added to immobilized rGFRα1 with purified $hRET^{ECD}$ added subsequently. The mTC was eluted by tobacco etch virus protease cleavage and was subsequently purified by size-exclusion chromatography. Zebrafish $RET^{ECD}$ (residues 1–626) and $zRET^{CLD1-4}$ (residues 1–502) were produced in insect cells as recombinant baculoviruses with a protein A tag using standard protocols. Zebrafish GFRα1a (residues 1–352) and zGDNF (residues 135–235) were prepared in the same manner. For zTC assembly, a similar protocol to mTC was followed with a final size-exclusion chromatography purification step.

### SAXS Data Collection and Processing

SAXS data were collected on the SWING beamline at synchrotron SOLEIL. Data were processed using both in-house and external SAXS software (see Supplemental Experimental Procedures). Data fitting used GNOM (Svergun, 1992) and ab initio models came from DAMMIF (Franke and Svergun, 2009) and DAMAVER (Volkov and Svergun, 2003).

#### *Epitope Mapping of mAbs and ELISA to Measure mAb Epitope Accessibility*

The locations of mAb epitopes recognized within $hRET^{ECD}$ were determined by either immuno-dot-blotting (for 1D9) or by peptide arrays spotted onto cellulose membranes (m123, 93A, and 421R25). An ELISA assay was employed to measure antibody binding to $hRET^{ECD}$, GDNF-GFRα1, or mTC as previously described (Kjaer and Ibáñez, 2003b).

#### *Electron Microscopy and Single-Particle Analysis Methods*

Molecular images of the mTC and $zTC^{min}$ complexes were recorded after negative staining using an FEI Tecnai TF20 electron microscope operating at 200 kV and were used to determine the 3D structures by single-particle analysis procedures. A structural model of the mTC complex was built by fitting atomic coordinates from published crystal structures and the SAXS model obtained in this study. Further details are given in the Supplemental Information.

## ACCESSION NUMBERS

A negative-stain EM map for the mTC has been deposited in the EMDataBank under accession code EMD-2712 and EMD-2713 for the zTC. The respective coordinates for the EM-based structural model are deposited in the Protein Data Bank under ID code 4ux8.

## SUPPLEMENTAL INFORMATION

Supplemental Information includes Supplemental Experimental Procedures, six figures, and two tables and can be found with this article online at http://dx.doi.org/10.1016/j.celrep.2014.08.040.

## AUTHOR CONTRIBUTIONS

K.M.G., S.K., and N.Q.M. designed the study. K.M.G. prepared the zTC complex and carried out all the SAXS and EM experiments on the mTC and zTC complexes. S.K. prepared the mTC complex, characterized the antibody epitopes, and performed the ELISA assays. K.M.G. and F.B. processed and interpreted the EM structural models. P.P.K. purified zGDNF-GFRα1 mutants and performed the biochemical assays. K.M.G., A.N., and E.M.B. generated zGDNF-GFRα1 mutants and expression constructs. A.G.P. assisted with the SAXS data acquisition, processing, and interpretation. R.G. assisted with recombinant baculovirus production. M.S. provided large quantities of 1D9 monoclonal antibody. E.P.M. assisted the mTC single-particle reconstruction and interpretation. K.M.G., S.K., F.B., E.P.M., and N.Q.M. interpreted results and wrote the paper.

## ACKNOWLEDGMENTS

We thank members of the N.Q.M. laboratory for helpful discussions and comments on the manuscript. K.M.G. was funded by a Cancer Research UK studentship to N.Q.M. Work in the N.Q.M. laboratory is supported by CR-UK core funding to the London Research Institute. E.P.M. is funded by Cancer Research UK programme grant C12209/A16749. We thank Pierre Roblin

and Javier Perez for access and assistance with performing the SAXS experiments on the SAXS beamline at Soleil. We thank Paula da Fonseca for help and advice on image processing and Annabel Borg for help with baculovirus production. We thank Tiffany Heanue and Vassilis Pachnis, NIMR, for the zebrafish RET construct, and both zebrafish GDNF and GFRα1a cDNAs were kindly provided by Iain Shepherd, Emory University. We also thank Professor Yvonne Jones, Oxford, for the GST-endoglycosidase F1 construct and Nicola O'Reilly for SPOT membrane peptide arrays.

Received: June 13, 2014
Revised: August 4, 2014
Accepted: August 17, 2014
Published: September 18, 2014

## REFERENCES

Airaksinen, M.S., and Saarma, M. (2002). The GDNF family: signalling, biological functions and therapeutic value. Nat. Rev. Neurosci. *3*, 383–394.

Amiel, J., Sproat-Emison, E., Garcia-Barcelo, M., Lantieri, F., Burzynski, G., Borrego, S., Pelet, A., Arnold, S., Miao, X., Griseri, P., et al.; Hirschsprung Disease Consortium (2008). Hirschsprung disease, associated syndromes and genetics: a review. J. Med. Genet. *45*, 1–14.

Amoresano, A., Incoronato, M., Monti, G., Pucci, P., de Franciscis, V., and Cerchia, L. (2005). Direct interactions among Ret, GDNF and GFRalpha1 molecules reveal new insights into the assembly of a functional three-protein complex. Cell. Signal. *17*, 717–727.

Anders, J., Kjar, S., and Ibáñez, C.F. (2001). Molecular modeling of the extracellular domain of the RET receptor tyrosine kinase reveals multiple cadherin-like domains and a calcium-binding site. J. Biol. Chem. *276*, 35808–35817.

Boulanger, M.J., Bankovich, A.J., Kortemme, T., Baker, D., and Garcia, K.C. (2003). Convergent mechanisms for recognition of divergent cytokines by the shared signaling receptor gp130. Mol. Cell *12*, 577–589.

Brasch, J., Harrison, O.J., Honig, B., and Shapiro, L. (2012). Thinking outside the cell: how cadherins drive adhesion. Trends Cell Biol. *22*, 299–310.

Brozzo, M.S., Bjelić, S., Kisko, K., Schleier, T., Leppänen, V.M., Alitalo, K., Winkler, F.K., and Ballmer-Hofer, K. (2012). Thermodynamic and structural description of allosterically regulated VEGFR-2 dimerization. Blood *119*, 1781–1788.

Ciatto, C., Bahna, F., Zampieri, N., VanSteenhouse, H.C., Katsamba, P.S., Ahlsen, G., Harrison, O.J., Brasch, J., Jin, X., Posy, S., et al. (2010). T-cadherin structures reveal a novel adhesive binding mechanism. Nat. Struct. Mol. Biol. *17*, 339–347.

Franke, D., and Svergun, D.I. (2009). DAMMIF, a program for rapid ab-initio shape determination in small-angle scattering. J. Appl. Cryst. *42*, 342–346.

Ibáñez, C.F. (2013). Structure and physiology of the RET receptor tyrosine kinase. Cold Spring Harb. Perspect. Biol. *5*, pii: a009134.

Kjaer, S., and Ibáñez, C.F. (2003a). Intrinsic susceptibility to misfolding of a hot-spot for Hirschsprung disease mutations in the ectodomain of RET. Hum. Mol. Genet. *12*, 2133–2144.

Kjaer, S., and Ibáñez, C.F. (2003b). Identification of a surface for binding to the GDNF-GFR alpha 1 complex in the first cadherin-like domain of RET. J. Biol. Chem. *278*, 47898–47904.

Kjaer, S., Kurokawa, K., Perrinjaquet, M., Abrescia, C., and Ibáñez, C.F. (2006). Self-association of the transmembrane domain of RET underlies oncogenic activation by MEN2A mutations. Oncogene *25*, 7086–7095.

Kjaer, S., Hanrahan, S., Totty, N., and McDonald, N.Q. (2010). Mammal-restricted elements predispose human RET to folding impairment by HSCR mutations. Nat. Struct. Mol. Biol. *17*, 726–731.

Lemmon, M.A., and Schlessinger, J. (2010). Cell signaling by receptor tyrosine kinases. Cell *141*, 1117–1134.

Mulligan, L.M. (2014). RET revisited: expanding the oncogenic portfolio. Nat. Rev. Cancer *14*, 173–186.

Parkash, V., Leppänen, V.M., Virtanen, H., Jurvansuu, J.M., Bespalov, M.M., Sidorova, Y.A., Runeberg-Roos, P., Saarma, M., and Goldman, A. (2008). The structure of the glial cell line-derived neurotrophic factor-coreceptor complex: insights into RET signaling and heparin binding. J. Biol. Chem. *283*, 35164–35172.

Salvatore, G., Nagata, S., Billaud, M., Santoro, M., Vecchio, G., and Pastan, I. (2002). Generation and characterization of novel monoclonal antibodies to the Ret receptor tyrosine kinase. Biochem. Biophys. Res. Commun. *294*, 813–817.

Santoro, M., Carlomagno, F., Romano, A., Bottaro, D.P., Dathan, N.A., Grieco, M., Fusco, A., Vecchio, G., Matoskova, B., Kraus, M.H., et al. (1995). Activation of RET as a dominant transforming gene by germline mutations of MEN2A and MEN2B. Science *267*, 381–383.

Schedl, A. (2007). Renal abnormalities and their developmental origin. Nat. Rev. Genet. *8*, 791–802.

Schlee, S., Carmillo, P., and Whitty, A. (2006). Quantitative analysis of the activation mechanism of the multicomponent growth-factor receptor Ret. Nat. Chem. Biol. *2*, 636–644.

Scott, R.P., and Ibanez, C.F. (2001). Determinants of ligand binding specificity in the glial cell line-derived neurotrophic factor family receptor alpha S. J. Biol. Chem. *276*, 1450–1458.

Stauber, D.J., Debler, E.W., Horton, P.A., Smith, K.A., and Wilson, I.A. (2006). Crystal structure of the IL-2 signaling complex: paradigm for a heterotrimeric cytokine receptor. Proc. Natl. Acad. Sci. USA *103*, 2788–2793.

Strauss, J.D., and Wagenknecht, T. (2013). Structure of glutaraldehyde cross-linked ryanodine receptor. J. Struct. Biol. *181*, 300–306.

Svergun, D.I. (1992). Determination of the regularization parameter in indirect-transform methods using perceptual criteria. J. Appl. Cryst. *25*, 495–503.

Treanor, J.J., Goodman, L., de Sauvage, F., Stone, D.M., Poulsen, K.T., Beck, C.D., Gray, C., Armanini, M.P., Pollock, R.A., Hefti, F., et al. (1996). Characterization of a multicomponent receptor for GDNF. Nature *382*, 80–83.

Trupp, M., Arenas, E., Fainzilber, M., Nilsson, A.-S., Sieber, B.-A., Grigoriou, M., Kilkenny, C., Salazar-Grueso, E., Pachnis, V., and Arumäe, U. (1996). Functional receptor for GDNF encoded by the c-ret proto-oncogene. Nature *381*, 785–789.

van Weering, D.H., Moen, T.C., Braakman, I., Baas, P.D., and Bos, J.L. (1998). Expression of the receptor tyrosine kinase Ret on the plasma membrane is dependent on calcium. J. Biol. Chem. *273*, 12077–12081.

Volkov, V.V., and Svergun, D.I. (2003). Uniqueness of ab initio shape determination in small-angle scattering. J. Appl. Cryst. *36*, 860–864.

Waguespack, S.G., Rich, T.A., Perrier, N.D., Jimenez, C., and Cote, G.J. (2011). Management of medullary thyroid carcinoma and MEN2 syndromes in childhood. Nat. Rev. Endocrinol. *7*, 596–607.

Wang, X., Rickert, M., and Garcia, K.C. (2005). Structure of the quaternary complex of interleukin-2 with its alpha, beta, and gammac receptors. Science *310*, 1159–1163.

Wang, X., Baloh, R.H., Milbrandt, J., and Garcia, K.C. (2006). Structure of artemin complexed with its receptor GFRalpha3: convergent recognition of glial cell line-derived neurotrophic factors. Structure *14*, 1083–1092.